Complex power distribution analysis in plates covered with passive constrained layer damping patches

A. Castel[a,*], A. Loredo[a], A. El Hafidi[a], B. Martin[b]

[a]*DRIVE, Université de Bourgogne, 49 rue Mlle Bourgeois, 58027 Nevers, France*
[b]*ICB, Université de Bourgogne, 49 rue Mlle Bourgeois, 58027 Nevers, France*

Abstract

The vibration of a plate partially covered with a passive constrained layer damping (PCLD) patch is studied from an energetic point of view. The damped plate is excited by an acoustic plane wave. The study is done with a numerical two-dimensional multilayer plate model. Results of the present model are compared to those obtained with three-dimensional finite element models. It is shown that the present model gives accurate results, even for the layer's inner behavior. It is less expansive in terms of computational cost; hence, it can simulate efficiently the structure for higher frequencies. Mathematical formulas for complex mechanical power are presented, and the link with strain and kinetic energies and dissipated power is detailed. Both local and global complex power balance are established, and corresponding expressions for the discretized problem are formulated. Conservative and dissipative powers are studied for the PCLD damped plate. After a global balance analysis versus frequency, a local study has been carried out in order to quantify the relative contribution of the components of strain and stress tensors to the total strain energy and dissipated power; the individual layer's contributions is also investigated. The in-plane distributions of powers are mapped, showing the location where dissipative phenomenon occurs and where strain energy is stored. Finally, three criteria based on the previous power quantities are proposed in order to quantify the mechanical damping efficiency of the patch.

Keywords: Complex power, patch, vibration, plate, damping, PCLD

1. Introduction

Passive constrained layer damping (PCLD) patches have been widely used since they were first introduced in 1939 by a British patent [1] for damping vibration in the automotive industry. Nowadays they remain an easy, cheap, and efficient way to reduce vibration and noise in a structure. For years, it has been used almost exclusively in the aeronautic industry; however, Rao [2] recently presented many new fields of applications of these treatments. Since the 1950's, many papers have presented studies of vibration damping of plates and beams by means of constrained layer damping devices. Most of these papers deal with plates fully covered with a PCLD treatment, which can be considered as sandwich plates. However, in the case of partial treatment of the plate, definite optimization of the patches layout is not established yet. Amongst the existing optimization algorithms, Zheng [3] presents a comparative study of four of them: a sub-problem approximation method, a first order optimization method, a sequential quadratic programming algorithm, and a genetic algorithm. The disadvantage of those iterative optimization algorithms is their high computation cost; therefore, most of them are limited to two-dimensional beam treatments. Other algorithms, such as gradient based methods developed by Lee [4] or Alvelid [5] and cellular automata developed by Chia [6, 7], were applied; yet, no algorithm led to a definite general design rule regarding the layout of the damping patches.

Numerical simulation of structural vibrations is classically carried out by means of displacement approaches. The Finite Element Method (FEM) has been extensively used for these studies. Indeed, this method is particularly efficient to study the vibrational behavior of rods, beams, plates, shells, solids and any assembly of

---

*Corresponding author
   Email addresses: `alexis.castel@u-bourgogne.fr` (A. Castel), `alexandre.loredo@u-bourgogne.fr` (A. Loredo),
`ali.el-hafidi@u-bourgogne.fr` (A. El Hafidi), `bruno.martin@u-bourgogne.fr` (B. Martin)

such elements, giving the possibility to study complex structures like automotive, aircraft, train or ship bodies, engines, buildings, wind turbines, etc. Nevertheless, the mesh of the structure must be sufficiently refined to let the shape functions of elements match the displacement field. When the wavelength is small compared to the dimensions of the studied structures, the use of a lot of elements and degrees of freedom is necessary. Then the computation cost can be very high, sometimes so much that the study is not feasible any more.

As an alternative to displacement-based approaches, methods based on energy or power were proposed. Statistical energy analysis (SEA)[8] is a method suitable to predict space- and frequency-averaged behavior of structures when the modal density is high, which generally corresponds to small wavelength/dimensions ratios. The SEA method is different from the FEM for at least two reasons: the SEA method solves a –relatively small– set of scalar energy balance equations, and is based upon statistical assumptions concerning distribution of energy versus modes and/or substructures; the FEM solves a –relatively big– system of linear equations corresponding to the discretization of partial differential equations (PDE) in a continuous media (the structure's domain) and is of deterministic nature. Another class of methods, the power flow analysis (PFA) [9], in which unknowns are powers, solves a heat conduction type PDE in the structure's domain. Hence, this approach can be formulated with the help of classical PDE solving tools, like the FEM. The PFA method has been applied to rods, beams [10, 11], and to one-layer plates [12]. However, the required power diffusion equations seem to be difficult to formulate for heterogeneous structures. Nevertheless, these methods emphasize the relevance of the power flow concept for the study of damped structures.

Energies, powers, and energy flow can also be computed from a classical displacement study and can improve the comprehension of the damping of complex structures as shown by Pavic [13, 14]. The aim of this paper is to present PCLD treatments from an energetic point of view, which could be a help for the design of the optimal layout of the patches. In this study, a PCLD damped plate is studied with the help of a model [15] based upon a zig-zag type plate theory [16] and the Rayleigh-Ritz method. Formulas that link the complex mechanical power to the time-averaged strain energy and to the time-averaged dissipated power are presented. The setting of a local and a global power balance is detailed. Formulas for computing all these quantities from matrices and vectors of the discretized problem are presented. These formulas are used to investigate the mechanism of damping. Agreement of the results, given by the studied model, is shown by comparison with two other FEM simulations: a classical three-dimensional study carried out with the Cast3m FEM software and a study realized with the shell elements of the code ACTRAN. Dissipative and conservative parts of the mechanical power are examined in several ways: global balance, global bending/shear repartition in each layer, and two dimensional spatial repartition. Based upon the global power balance, generalized damping factors are proposed.

2. Present plate model

2.1. Considerations on plate models

A plate damped with PCLD patches is formally a multilayered plate with spatial inhomogeneities. Both static and dynamic behaviors of such structures have been studied in early works [17, 18], and, because of their complexity, they have been and still are extensively studied, causing the developments of many models [19, 20]. The goal of all these models is to reduce the plate to a two-dimensional structure by eliminating the thickness dimension; this implies the consideration of bending (and possibly shear) generalized displacements and forces. The classical laminate theory (CLT) is efficient for thin plates, and the (first-order) shear deformation theory (SDT) is appropriate for plates of moderate thickness. For the SDT, shear correction factors have been proposed by various authors [21–24] in order to take into account the transverse shear stresses variations, which strongly depends on the adjacent layer modulus and the laminate stacking sequence. These works gave different results, which points out the difficulty of the task, especially when dealing with the dynamic behavior. Higher order shear deformation theories [25–27] and also alternative approaches like the so called zig-zag theories [19, 28] have been formulated. All these models are perfectly compatible with the finite element method (FEM) or with Rayleigh-Ritz approaches. Commercial finite element (FE) codes classically propose CLT and SDT based elements. However, plates with PCLD patches exhibit a very high elastic modulus ratio between the elastic layers and the viscoelastic one, which is not compatible with these classical plate models. For this study, the SDT (with or without shear correction factors) has been tested and compared to other approaches including the present model, and a poor agreement was found (results are not presented in this paper). On the contrary,

the present model is based upon a zig-zag type model [16], and it is shown in this document that it is very accurate for the PCLD problem.

2.2. Specificities of the present model

The present model, as described by Loredo [15], allows one to simulate the behavior of a rectangular multilayered plate with one or several multilayered patches. It is based on an out-of-plane assumed displacement field obtained by means of kinematic and static considerations. This approach was used in the early work of Sun & Whitney [16] for multilayered plates and has been used later for vibroacoustical purposes by Guyader and Lesueur [29].

It is a two-dimensional plate model with the five classical displacement unknowns, but it differs from classical laminate theories CLT and SDT because the assumed displacement variation, with respect to z, is piecewise linear. This is the result of writing continuities of both displacements and shear stresses at each interface, as shown below. For practical reasons, the displacement field of each layer $\ell \in [2..n]$ is linked to the displacement field of the first layer. Thicknesses and elevations for an n layer material are presented in figure 1. The displacement field in each layer is written as follows,

$$\begin{cases} u_\alpha^\ell(x,y,z) = u_\alpha^\ell(x,y,z^\ell) + (z^\ell - z)(u_{3,\alpha}^1(x,y) - \gamma_{\alpha 3}^\ell(x,y)) \\ u_3^\ell(x,y,z) = u_3^1(x,y) \end{cases} \tag{1}$$

where greek indices stand for in-plane quantities and take values 1 or 2, superscript ℓ stands for the ℓ-th layer and superscript 1 stands for the first layer for which all will be related, $\gamma_{\alpha 3}^\ell(x,y)$ are the transverse (engineering) shear strains, and z^ℓ is the elevation of the layer ℓ.

With these assumptions, the transverse displacement u_3 and the transverse shear strains $\gamma_{\alpha 3}^\ell$ are constant within each layer with respect to the z-coordinate. Therefore, transverse shear stresses will also be constant in each layer. According to these remarks, the conditions that are enforced reduce to:

- the continuity of displacements

$$\{ u_\alpha^\ell(x,y,z^\ell + h^\ell/2) = u_\alpha^{\ell+1}(x,y,z^{\ell+1} - h^{\ell+1}/2) \tag{2}$$

- the continuity of transverse shear stresses

$$\{ \sigma_{\alpha 3}^\ell = \sigma_{\alpha 3}^{\ell+1} \tag{3}$$

Equations (2) and (3) allow linking the displacements field in the $(\ell+1)$-th layer with the one of the ℓ-th layer, and, recursively, it can be linked to the displacement field of the first layer, following a process detailed in reference [29].

As the first layer is common to the uncovered and covered parts of the plate, all the displacements in the multilayered structure are known in terms of the first layer's displacement field, including only the five classical plate unknowns: three displacements u_i^1 and two rotations $\varphi_\alpha^1 = u_{3,\alpha}^1 - \gamma_{\alpha 3}^1$.

The construction of the discrete motion equation system is achieved by the Rayleigh-Ritz method. Various boundary conditions and external solicitations can be considered, as it is presented in detail in reference [15].

3. Model aptitude – Comparisons with FE models

3.1. Studied damped plate

Throughout this study, the same test case is used. A rectangular aluminum plate, with dimensions $a = 0.6$ m, $b = 0.5$ m, and thickness $h = 1$ mm, is excited with a plane wave traveling towards the plate with incidence angles $\theta = 45°$, $\varphi = 45°$, and amplitude 1 Pa (see figure 2 for corresponding definitions). The plate is clamped on its four sides. Aluminum material has the following properties: Young's modulus $E = 7.24 \times 10^{10}$ Pa, density $\rho_s = 2780$ kg m^{-3}, Poisson's ratio $\nu = 0.33$, and loss factor $\eta_s = 0.005$. A centered two layer PCLD patch with dimensions $a_p = 0.3795$ m, $b_p = 0.3162$ m covers 40% of the total area of the plate. The first layer made of a viscoelastic material ISD 112 is 0.2 mm thick with a density of 1015 kg m^{-3} and Poisson's ratio of 0.45. Table 1 presents the frequency dependence of the viscoelastic material properties for a given temperature. For computational purposes, an interpolation has been used, and the corresponding formulas are given in the appendix. The constraining layer is 0.2 mm thick and is made of the same aluminum as the plate.
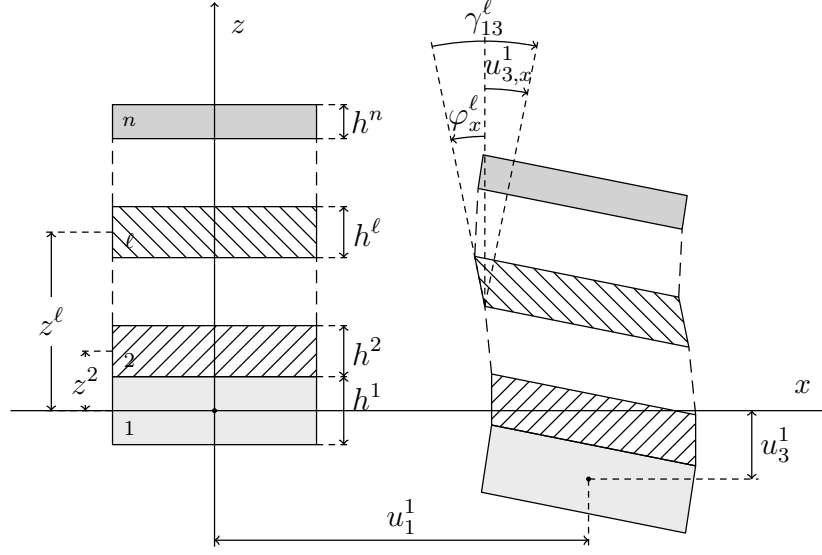
Figure 1: Geometrical parameters of the multilayer structure (represented on the left side in an undeformed state) and displacements (represented on the right side after deformation).
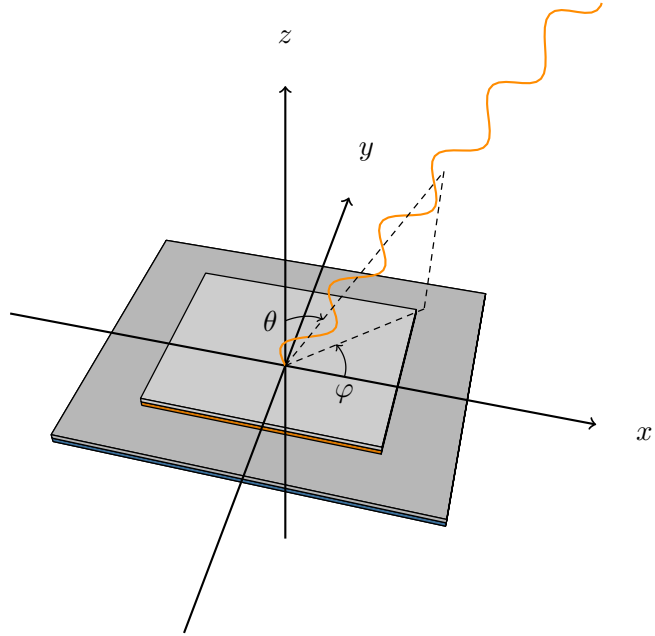

Figure 2: View of a patched plate submitted to an acoustic plane-wave, showing the definition of the angles of incidence θ and φ.

Table 1: Frequency dependence of the mechanical properties of the viscoelastic material ISD 112 ($T = 25°C$).

Frequency (Hz)	Young's Modulus (Pa)	Loss factor
10	7.28×10^5	0.90
100	2.34×10^6	1.00
500	5.20×10^6	1.00
1000	7.28×10^6	0.90
2000	9.88×10^6	0.80
3000	1.17×10^7	0.75
4000	1.38×10^7	0.70

3.2. Comparison with three-dimensional FE models

To verify the accuracy of the present model, a comparison is made with two finite element simulations. The two associated finite element models are of three-dimensional type: the plate, the viscoelastic and the constraining layers are each discretized with one element in the thickness. These two models use the same 20-node hexahedron support element, but the chosen element in the ACTRAN code implements a shell formulation; whereas, the chosen element in the Cast3m code only uses the three-dimensional elasticity equations and then does not involve any kinematic hypothesis.

Figure 3 shows the evolution of the mean square velocity $\langle V^2 \rangle$ versus the number of degrees of freedom (DOF) for the two frequencies of 400 and 3000 Hz. For the 400 Hz case of figure 3(a), it is shown that convergence is achieved with more than ten times less DOF for the shell formulation than for the three-dimensional formulation and that the two-dimensional present model is able to give the same result with two times less DOF than the the shell formulation. For the 3000 Hz case of figure 3(b), the same tendency is observed, but convergence with the three-dimensional formulation could not be achieved on our computer since the required number of DOF exceeds its memory capacities[1].

Figure 4 presents the evolution of the mean square velocity $\langle V^2 \rangle$ versus frequency for the three models. The calculations for the three-dimentional model have been stopped at 800 Hz, since above this frequency, the required number of DOF to ensure convergence makes computation time longer than one hour for every frequency point on our computer.

3.3. Higher frequency comparison with a two-dimensional FE beam model

In order to work at higher frequencies, the size of the system must be increased, which cannot be done easily for the two three-dimensional approaches as seen before. On the contrary, the two-dimensional present model can work at higher frequencies.

To allow a verification of the model at higher frequencies, a beam model using the same displacement field has been realized by setting the maximum order of the base in the modifiedwidth direction to zero (allowing only a constant displacement). Then, a comparison of this model is made with a two-dimensional finite element beam model, implemented with Cast3m (plane strain condition is applied).

For both models, the same test case is simulated: a beam with length $a = 0.6$ m and thickness $h = 1$ mm is excited with an acoustic plane wave of incidence angle $\theta = 45°$ and amplitude 1 Pa. The beam is covered with a centered two-layer PCLD patch with dimension $a_p = 0.3795$ m and same structure and characteristics as in the preceding plate studies.

For the present model, the maximum order of the base is set to 100 in the length direction; this value is obtained after a convergence study at 10 kHz. The two-dimensional finite element mesh chosen after a convergence study is made of 3000×10 elements for the base plate and 1898×2 elements for the patch (there is one element per layer on the thickness direction).

Simulation is carried out over the $10 - 10000$ Hz frequency range. Figure 5 presents the evolution of the mean square velocity $\langle V^2 \rangle$ versus frequency for the two models. It shows that the present model agrees with the finite element one up to 5 kHz, and results in the $5 - 10$ kHz range are quite similar. Note that this two-dimensional finite element model takes into account deformation along the thickness direction (ε_{zz} can be different from zero).

---

[1]Simulations performed on an Intel(R) Xeon(R) W3550 with 8 gigabyte of RAM
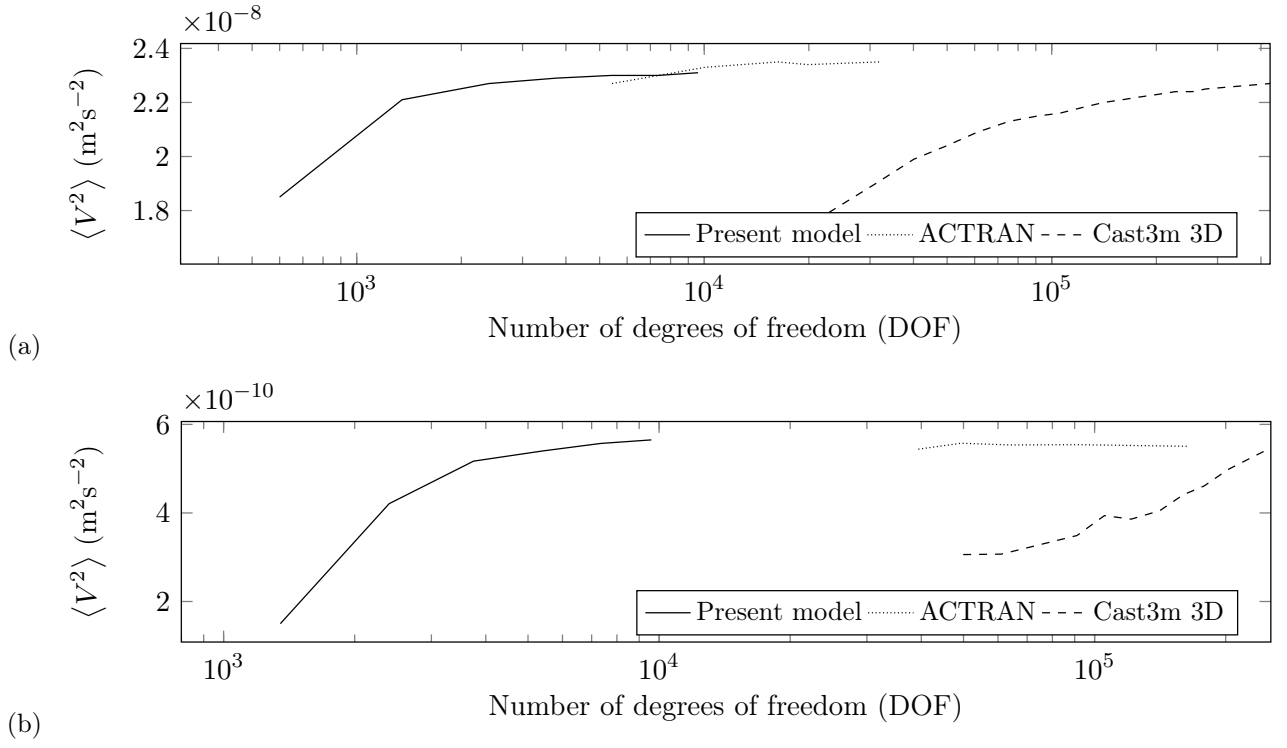
(a)

(b)

Figure 3: Convergence study for the three models: evolution of the mean square velocity $\langle V^2 \rangle$ at 400 Hz (a) and 3000 Hz (b) versus the number of degrees of freedom.
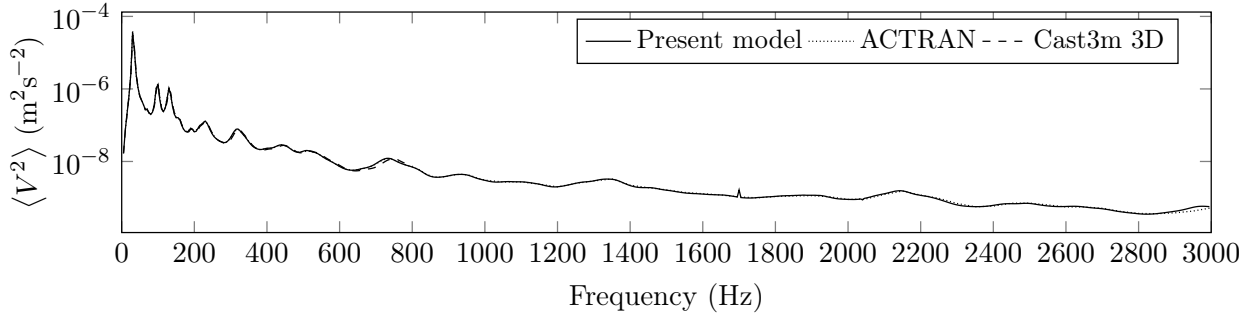

Figure 4: Evolution of the mean square velocity $\langle V^2 \rangle$ for the three models.
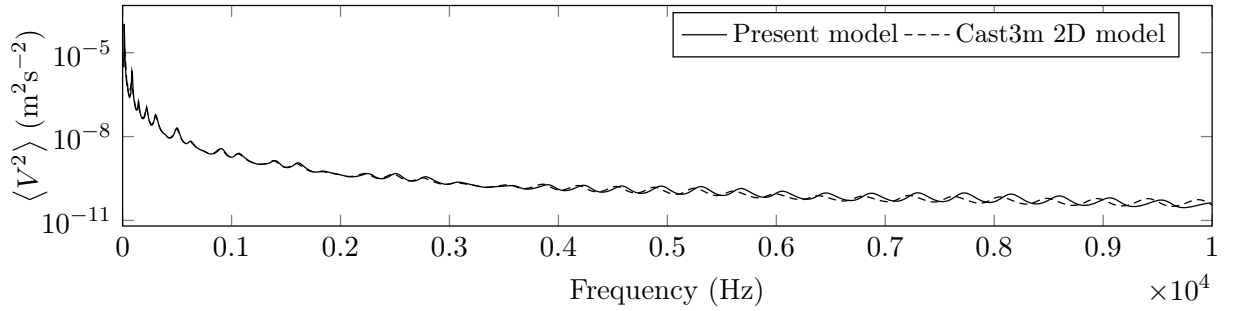

Figure 5: Mean square velocity $\langle V^2 \rangle$ for the beam corresponding problem: comparison of the present model to a two-dimensional plane deformation finite element model.

3.4. Discussion

In this section, it is shown that finite element computations using a three-dimensional elasticity formulation is not suitable to study PCLD patch problems because it needs a very refined mesh and then generates huge systems of equations. Three-dimensional finite elements with shell formulation gives better results. These two approaches were implemented in order to get a reference solution, and it is shown that they agree very well as long as the convergence can be achieved.

Two-dimensional finite elements using classical multilayer first order shear deformation theory have been tested, with and without shear correction coefficients, but a poor agreement was found with the three-dimensional models (this study is not presented here). On the other hand, the present model, which is also a multilayer plate model, gives good results compared to the three-dimensional plate model, while keeping the good performance of a two-dimensional model. Furthermore, it is shown by comparison with a two-dimensional finite element beam model that it can manage studies with higher wavenumbers. This shows that the assumed displacement/stress field of the present model is very accurate for the PCLD problem.

4. Complex mechanical power

4.1. Link between classical energies and complex power

It is assumed in this study that the displacements are small. Considered materials are viscoelastic with viscous damping. The damping factor η can depend on the frequency, but, in this section, this dependence is not considered because computations are done for a given frequency. Materials are supposed to obey to the anisotropic generalization of the Kelvin-Voigt model,

$$\sigma_{ij} = \sigma_{ij}^{\mathrm{el}} + \sigma_{ij}^{\mathrm{vi}} = C_{ijkl}\varepsilon_{kl} + \eta_{ijkl}\dot{\varepsilon}_{kl}$$

$$\text{with } C_{ijkl} = C_{ijlk} = C_{klij} \quad \text{and} \quad \eta_{ijkl} = \eta_{ijlk} = \eta_{klij} \tag{4}$$

where $\dot{\varepsilon}_{kl}$ denotes the time derivative of ε_{kl}, the second order Cauchy's stress tensor $\boldsymbol{\sigma}$ is the sum of two symmetric second order tensors $\boldsymbol{\sigma}^{\mathrm{el}}$ and $\boldsymbol{\sigma}^{\mathrm{vi}}$, which stand respectively for the *elastic* and *viscous* contributions for stresses.

When dealing with damped structures, it can be useful to access to spatial repartitions of the kinetic energy $e_k(t)$, the strain energy $e_s(t)$, and the dissipated power densities $p_d(t)$. Let us define these time dependent quantities:

$$e_k(t) = \frac{1}{2}\rho v_i(t)v_i(t) \quad e_s(t) = \frac{1}{2}\sigma_{ij}^{\mathrm{el}}(t)\varepsilon_{ij}(t) = \frac{1}{2}C_{ijkl}\varepsilon_{kl}(t)\varepsilon_{ij}(t) \quad p_d(t) = \sigma_{ij}^{\mathrm{vi}}(t)\dot{\varepsilon}_{ij}(t) = \eta_{ijkl}\dot{\varepsilon}_{kl}(t)\dot{\varepsilon}_{ij}(t) \tag{5}$$

As periodically loaded damped structures are commonly treated using complex quantities, it is interesting to deal with complex powers, which, as will be seen below, give natural access to time-averages of the above quantities. In addition, it is possible to write both local and global power balances involving the complex incoming power $\tilde{P}_{\mathrm{inc}}$, and time-averages of the dissipated power, the kinetic energy, and the strain energy. Sections 4.2 and 4.3 are devoted to this point.

In complex form, the material behavior law (4) becomes:

$$\tilde{\sigma}_{ij} = C_{ijkl}\tilde{\varepsilon}_{kl} + \mathrm{j}\,\omega\eta_{ijkl}\tilde{\varepsilon}_{kl} \tag{6}$$

Time-averaged quadratic quantities of formulas (5) can be built taking half of the real part of the corresponding hermitian products:

$$\langle e_k(t)\rangle = \frac{1}{4}\rho\tilde{v}_i^*\tilde{v}_i \qquad \langle e_s(t)\rangle = \frac{1}{4}\mathrm{Re}(\tilde{\sigma}_{ij}^{\mathrm{el}*}\tilde{\varepsilon}_{ij}) \qquad \langle p_d(t)\rangle = \frac{1}{2}\mathrm{Re}(\mathrm{j}\,\omega\tilde{\sigma}_{ij}^{\mathrm{vi}*}\tilde{\varepsilon}_{ij}) \tag{7}$$

The Re symbol has been omitted for the kinetic energy because this quadratic term is obviously real. The major symmetry of the fourth order tensors in the above behavior law implies that $\tilde{\sigma}_{ij}^{\mathrm{el}*}\tilde{\varepsilon}_{ij}$ is real and $\tilde{\sigma}^{\mathrm{vi}*}\tilde{\varepsilon}_{ij}$ is imaginary. Then, the remaining Re symbols in equation (7) can also be omitted. Indeed:

$$\langle e_k(t)\rangle = \frac{1}{4}\rho\tilde{v}_i^*\tilde{v}_i \qquad \langle e_s(t)\rangle = \frac{1}{4}\tilde{\sigma}_{ij}^{\mathrm{el}*}\tilde{\varepsilon}_{ij} \qquad \langle p_d(t)\rangle = \frac{1}{2}\mathrm{j}\,\omega\tilde{\sigma}_{ij}^{\mathrm{vi}*}\tilde{\varepsilon}_{ij} \tag{8}$$

It is also interesting to remark at this time that:

$$\frac{1}{2}\tilde{\sigma}_{ij}^*\tilde{\varepsilon}_{ij} = \frac{1}{2}(\tilde{\sigma}_{ij}^{\mathrm{el}*}\tilde{\varepsilon}_{ij} + \tilde{\sigma}_{ij}^{\mathrm{vi}*}\tilde{\varepsilon}_{ij}) = 2\langle e_s(t)\rangle - \mathrm{j}\,\frac{1}{\omega}\langle p_d(t)\rangle \tag{9}$$

4.2. Local complex power balance

Let us start with the equilibrium equations of continuum mechanics:

$$\sigma_{ji,j} + \rho f_i^v = \rho \dot{v}_i \tag{10}$$

For the corresponding harmonic problem, the use of complex quantities leads to:

$$\tilde{\sigma}_{ji,j} + \rho \tilde{f}_i^v = \mathrm{j}\,\omega\rho\tilde{v}_i \tag{11}$$

The complex power balance is obtained by computing half of the hermitian product of equation (11) by $\{\tilde{v}_i\}$, which gives:

$$\frac{1}{2}\tilde{v}_i^*\tilde{\sigma}_{ji,j} + \frac{1}{2}\rho\tilde{v}_i^*\tilde{f}_i^v = \mathrm{j}\,\frac{1}{2}\omega\rho\tilde{v}_i^*\tilde{v}_i \tag{12}$$

Integration by parts of the first term leads to:

$$-\frac{1}{2}\tilde{v}_{i,j}^*\tilde{\sigma}_{ji} + \frac{1}{2}(\tilde{v}_i^*\tilde{\sigma}_{ji})_{,j} + \frac{1}{2}\rho\tilde{v}_i^*\tilde{f}_i^v = \mathrm{j}\,\frac{1}{2}\omega\rho\tilde{v}_i^*\tilde{v}_i \tag{13}$$

According to the symmetry of the stress tensor, one can write:

$$-\frac{1}{2}\tilde{D}_{ij}^*\tilde{\sigma}_{ji} + (\frac{1}{2}\tilde{v}_i^*\tilde{\sigma}_{ji})_{,j} + \frac{1}{2}\rho\tilde{v}_i^*\tilde{f}_i^v = \mathrm{j}\,\omega\frac{1}{2}\rho\tilde{v}_i^*\tilde{v}_i \tag{14}$$

where D_{ij} is the stretch rate tensor. For small strains, $D_{ij} = \dot{\epsilon}_{ij}$, which implies $\tilde{D}_{ij} = \mathrm{j}\,\omega\tilde{\epsilon}_{ij}$ for harmonic excitation. Introducing $\tilde{I}_j = \frac{1}{2}\tilde{v}_i^*\tilde{\sigma}_{ji}$ as the complex power flow vector[2], it follows:

$$\tilde{I}_{j,j} + \frac{1}{2}\rho\tilde{v}_i^*\tilde{f}_i^v = \mathrm{j}\,\omega\frac{1}{2}\rho\tilde{v}_i^*\tilde{v}_i + \mathrm{j}\,\frac{1}{2}\omega\tilde{\epsilon}_{ij}^*\tilde{\sigma}_{ji} \tag{15}$$

Replacing the terms of the right side with the help of formulas (8) and (9) gives the local complex power balance:

$$\tilde{I}_{j,j} + \frac{1}{2}\rho\tilde{v}_i^*\tilde{f}_i^v = \langle p_d(t)\rangle + 2\,\mathrm{j}\,\omega(\langle e_k(t)\rangle - \langle e_s(t)\rangle) \tag{16}$$

This equation can be split into its real and imaginary parts, leading to a system describing separately conservative and dissipative quantities. This splitting of the local power balance is not presented here, as a similar splitting concerning the global power balance will be presented in section 5.1, formula (26).

4.3. Global complex power balance

Integrating equation (16) over a domain $\mathcal{V}$ of boundary $\mathcal{S}$ using Ostrogradsky's theorem and the boundary conditions for the stress tensor, leads to the global complex plower balance,

$$\tilde{P}_{\mathrm{inc}} = \tilde{P}_{f^s} + \tilde{P}_{f^v} = \langle P_d(t)\rangle + 2\,\mathrm{j}\,\omega(\langle E_k(t)\rangle - \langle E_s(t)\rangle) \tag{17}$$

where $\tilde{P}_{\mathrm{inc}}$ is the complex incoming power, which is the sum of the complex powers of surface and body forces whose expressions are

$$\tilde{P}_{f^s} = \oint_{\mathcal{S}} \frac{1}{2}\tilde{v}_i^*\tilde{f}_i^s \mathrm{d}S \tag{18}$$

$$\tilde{P}_{f^v} = \int_{\mathcal{V}} \frac{1}{2}\tilde{v}_i^*\tilde{f}_i^v \mathrm{d}V \tag{19}$$

and $\langle P_d(t)\rangle$, $\langle E_k(t)\rangle$, and $\langle E_s(t)\rangle$ are integrals over $\mathcal{V}$ of $\langle p_d(t)\rangle$, $\langle e_k(t)\rangle$ and $\langle e_s(t)\rangle$ respectively.

---

[2]also called intensity vector

4.4. Corresponding discrete expressions

Discretization of equation (17) with a displacement formulation (e.g., using the Finite Element Method or the Rayleigh-Ritz method) gives a linear system of equations written with a mass matrix $\mathbf{M}$, a complex stiffness matrix $\tilde{\mathbf{K}}$, a generalized force vector $\tilde{\mathbf{f}}$, and unknowns, which are generalized displacements $\tilde{\mathbf{u}}$:

$$(\tilde{\mathbf{K}} - \omega^2 \mathbf{M})\tilde{\mathbf{u}} = \tilde{\mathbf{f}} \tag{20}$$

Usually, the $\tilde{\mathbf{f}}$ vector is the sum of the contributions of body $\tilde{\mathbf{f}}^v$ and surface $\tilde{\mathbf{f}}^s$ forces. The quantities of formulas (17) can then be expressed in terms of the discrete system quantities:

$$\tilde{P}_{f^s} = \oint_{\mathcal{S}} \frac{1}{2}\tilde{v}_i^* \tilde{f}_i^s \mathrm{d}S \qquad = -\frac{1}{2}\mathrm{j}\,\omega \tilde{\mathbf{u}}^{*\mathrm{T}} \tilde{\mathbf{f}}^s \tag{21}$$

$$\tilde{P}_{f^v} = \int_{\mathcal{V}} \frac{1}{2}\tilde{v}_i^* \tilde{f}_i^v \mathrm{d}V \qquad = -\frac{1}{2}\mathrm{j}\,\omega \tilde{\mathbf{u}}^{*\mathrm{T}} \tilde{\mathbf{f}}^v \tag{22}$$

$$\langle E_k(t)\rangle = \int_{\mathcal{V}} \frac{1}{4}\rho \tilde{v}_i^* \tilde{v}_i \mathrm{d}V \qquad = \frac{1}{4}\omega^2 \tilde{\mathbf{u}}^{*\mathrm{T}} \mathbf{M} \tilde{\mathbf{u}} \tag{23}$$

$$\langle E_s(t)\rangle = \int_{\mathcal{V}} \frac{1}{4}\mathrm{Re}(\tilde{\sigma}_{ij}^* \tilde{\varepsilon}_{ij}) \mathrm{d}V \quad = \frac{1}{4}\tilde{\mathbf{u}}^{*\mathrm{T}} \mathrm{Re}(\tilde{\mathbf{K}}) \tilde{\mathbf{u}} \tag{24}$$

$$\langle P_d(t)\rangle = \int_{\mathcal{V}} \frac{1}{4}\mathrm{Re}(\mathrm{j}\,\omega \tilde{\sigma}_{ij}^* \tilde{\varepsilon}_{ij}) \mathrm{d}V = \frac{1}{2}\omega \tilde{\mathbf{u}}^{*\mathrm{T}} \mathrm{Im}(\tilde{\mathbf{K}}) \tilde{\mathbf{u}} \tag{25}$$

5. Power analysis

5.1. Global power balance

To avoid excessive computation time, the refinements of the meshes have been set to $59 \times 49 \times 1 + 37 \times 31 \times 2$ for the Cast3m model (91104 DOF) and to $40 \times 33 \times 1 + 25 \times 21 \times 2$ for the ACTRAN model (42264 DOF). Calculations for the three-dimentional model have been stopped at 800 Hz for the same reason as explained in section 3.2. The powers $\langle P_d(t)\rangle$, $2\omega\langle E_k(t)\rangle$, and $2\omega\langle E_s(t)\rangle$ given by the three codes are plotted versus frequency in figure 6. This shows a satisfying agreement between the three simulations, despite the fact that they are based on different methods.

In order to verify the global power balance of equation (17), global energies and powers are computed with the corresponding vectors and matrices by means of the formulas of section 4.4. Then, we separate the real and the imaginary parts of the power balance, which gives the system:

$$\begin{cases} \mathrm{Re}(\tilde{P}_{f^s} + \tilde{P}_{f^v}) = \langle P_d(t)\rangle \\ \mathrm{Im}(\tilde{P}_{f^s} + \tilde{P}_{f^v}) = 2\omega(\langle E_k(t)\rangle - \langle E_s(t)\rangle) \end{cases} \tag{26}$$

These formulas have been tested for the present model over the frequency range $5 - 1200$ Hz. The relative error $\tilde{\epsilon}$ of the power balance has maximum real and imaginary values of $\mathrm{Re}(\epsilon) = 1.102 \times 10^{-8}$ and $\mathrm{Im}(\epsilon) = 1.206 \times 10^{-13}$ over the tested frequency range. This validates the formulas of section 4.4 and shows that the global complex power balance is accurately verified.

5.2. Contribution of tensor components to powers

It is possible to distinguish in each layer the contribution of different deformation modes. According to the restriction to orthotropic materials with symmetry axes coinciding with the reference frame, the contributions of the in-plane deformation (components 11, 22, and 12 of stress and strain tensors), of the xz transverse shear deformation (components 13), and of the yz transverse shear deformation (components 23) to the strain energy can be computed separately.

In table 2, these contributions are given for the considered structure and excitation at a frequency of 80 Hz for the dissipated power, $\langle P_d(t)\rangle$, and the *equivalent strain power*[3], $2\omega\langle E_s(t)\rangle$. For the considered structure, 80 Hz corresponds to a non modal frequency between the first two eigenfrequencies. A comparison with the three-dimensional finite element model shows satisfying agreement.

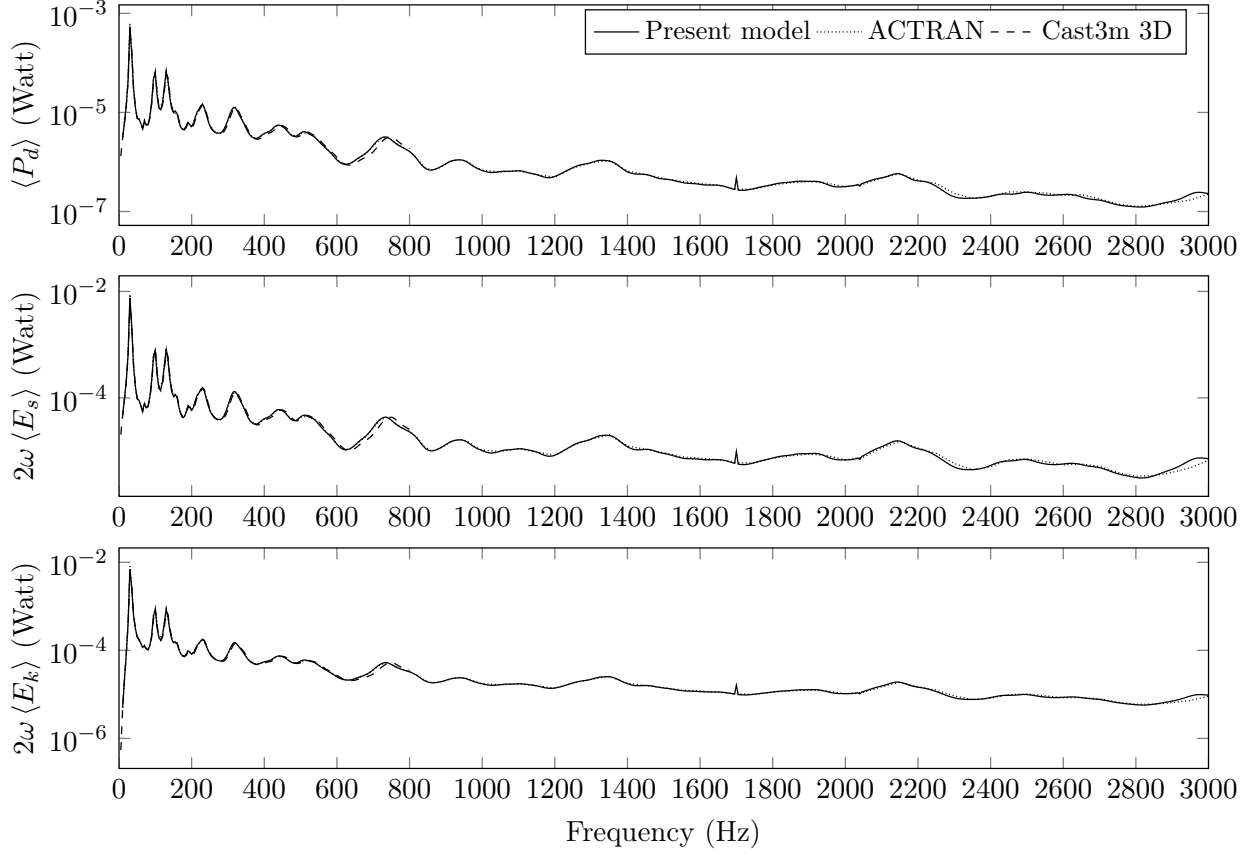[3]the power developed by internal elastic forces on a cycle is null

Figure 6: Powers $\langle P_d(t)\rangle$, $2\omega\,\langle E_k(t)\rangle$, and $2\omega\,\langle E_s(t)\rangle$ for three different models: the present model, the ACTRAN 3D shell FE model, and the Cast3m 3D FE model.

Table 2: Repartition over the different direction of space obtained with the Rayleigh Ritz method at 80 Hz.

Components	Present model $\langle P_d(t)\rangle$ (W)	Part	Cast3m 3D $\langle P_d(t)\rangle$ (W)	Part	Present model $2\omega\,\langle E_s(t)\rangle$ (W)	Part	Cast3m 3D $2\omega\,\langle E_s(t)\rangle$ (W)	Part
11 22 12 (33)	3.118×10^{-7}	5.4%	3.107×10^{-7}	5.7%	6.230×10^{-5}	92.0%	6.203×10^{-5}	92.2%
13	3.209×10^{-6}	56.0%	2.999×10^{-6}	54.7%	3.202×10^{-6}	4.7%	3.024×10^{-6}	4.5%
23	2.206×10^{-6}	38.5%	2.178×10^{-6}	39.7%	2.200×10^{-6}	3.2%	2.190×10^{-6}	3.3%
Total	5.726×10^{-6}		5.488×10^{-6}		6.770×10^{-5}		6.724×10^{-5}	
Layer	$\langle P_d(t)\rangle$ (W)	Part	$\langle P_d(t)\rangle$ (W)	Part	$2\omega\,\langle E_s(t)\rangle$ (W)	Part	$2\omega\,\langle E_s(t)\rangle$ (W)	Part
Base plate	2.477×10^{-7}	4.3%	2.585×10^{-7}	4.7%	4.953×10^{-5}	73.2%	5.171×10^{-5}	76.9%
Viscoelastic layer	5.415×10^{-6}	94.6%	5.177×10^{-6}	94.3%	5.395×10^{-6}	8%	5.158×10^{-6}	7.7%
Constraining layer	6.385×10^{-8}	1.1%	5.189×10^{-8}	1.0%	1.275×10^{-5}	18.9%	1.038×10^{-5}	15.4%
Total	5.727×10^{-6}		5.488×10^{-6}		6.767×10^{-5}		6.724×10^{-5}	

These results show clearly the importance of the transverse shear deformations of the viscoelastic layer for the damping and the importance of in-plane deformation of both elastic layers for the strain energy. Of course this is due to the relative position of each layer in the structure and to different Young's moduli of materials. The location of transverse shear deformation in the soft intermediate layer and of the in-plane deformation in the upper and lower rigid layers is not a surprising fact as it is common for sandwich structures. Note the strong contribution of the viscoelastic layer to damping: let us recall that Young's modulus of the viscoelastic material is (at this frequency) 35000 times lower than the Young modulus of aluminum. Despite a loss factor of 0.005 for the aluminum and 1.0 for the viscoelastic material, the viscoelastic layer is responsible for 94.6% of the dissipation of the whole structure, whereas it occupies only 6.9% of the volume, represents only 2.6% of the mass and covers 40% of the surface.

Note that the contribution of the transverse shear (components 13 and 23 of tensors) are strongly governed by the shape of the deformation, so they can vary with the frequency or the excitation, but the sum of them remains approximatively constant when frequency varies. Note also that the minor contribution of the transverse component (33) has been added to the in-plane contribution for the three-dimensional model.

This comparison with a three-dimensional finite element study shows that the present model, which can be classified as a zig-zag equivalent single layer model (based upon the classification given in [28]), is able to compute precise contributions of each layer and each deformation mode to conservative or dissipative power.

5.3. Power distribution over the surface

It is possible to derive the strains from the displacement field described in [16] and then compute local values of $\tilde{\varepsilon}(x,y,z)$ and $\tilde{\sigma}(x,y,z)$. Integration of equation (9) over the thickness and multiplication by $(\mathrm{j}\,\omega)$ leads to:

$$\frac{1}{2}\int_0^h \tilde{\sigma}_{ij}^*(x,y,z)\,\mathrm{j}\,\omega\tilde{\varepsilon}_{ij}(x,y,z)\mathrm{d}z = \int_0^h \langle p_d(x,y,z,t)\rangle\mathrm{d}z + 2\,\mathrm{j}\,\omega\int_0^h \langle e_s(x,y,z,t)\rangle\mathrm{d}z \tag{27}$$

which permits definition of the associated surface densities of powers, $\tilde{p}^s(x,y)$, $\langle\tilde{p}_d^s(x,y,t)\rangle$, and $2\omega\,\langle\tilde{e}_s^s(x,y,t)\rangle$:

$$\tilde{p}^s(x,y) = \langle p_d^s(x,y,t)\rangle + 2\,\mathrm{j}\,\omega\,\langle e_s^s(x,y,t)\rangle \tag{28}$$

For the system described in section 3, and the square velocity $\langle\dot{u}_3^2(t)\rangle = 1/2\,\omega^2\tilde{u}_3^*\tilde{u}_3$, the two powers $\langle p_d^s(x,y,t)\rangle$ and $2\omega\,\langle e_s^s(x,y,t)\rangle$ are mapped for two frequencies, 80 Hz and 850 Hz, and are presented in figures 7 and 8. The 850 Hz frequency has been added to explore the mid frequency range. It has been chosen since the patch seems to have a low efficiency according to criteria presented in section 6.

By comparing figures 7(a) and 7(c), we can notice a direct link between the mean square velocity and the location of the strain energy; however, figure 7(b) shows that the location of dissipated power is different from the location of conservative strain energy.

For a higher frequency, 850 Hz, we can conclude from figure 8 that the power associated with the conservative strain energy $2\omega\,\langle e_s^s(t)\rangle$ tends to be stored on the outside of the patched surface; conversely, the dissipated power $\langle p_d^s(t)\rangle$ seems to be lower than at 80 Hz. We can consider the patch not to be very efficient at this frequency; therefore, it is interesting to compute ratios presented in section 6.

It can also be seen that an asymmetry is visible, especially for the second case with the 850 Hz excitation. It is due to the direction of the incident acoustic plane-wave. Levels of energies are higher in the opposite corner to the provenance of the plane-wave. This can be explained by the fact that the incident plane wave creates a progressive plane wave in the plate, with a wavelength corresponding to the projection of the acoustic wavelength. This plane wave progresses in the same direction as the projection of the incident plane wave and brings energy to the opposite corner. This energy reflects off the boundaries but the damping makes the amount of reflected energy lower, explaining the observed asymmetry. This phenomenon has been observed for various incidence angles and various frequencies, and it is easier to see on animated plots. However, the presumed role of damping has not been investigated at this time.

This tool, displaying the energy distribution over the plate, brings a new aspect to the problem of optimal patch layout. This deterministic method allows a better understanding of how the pach damps the vibrations.
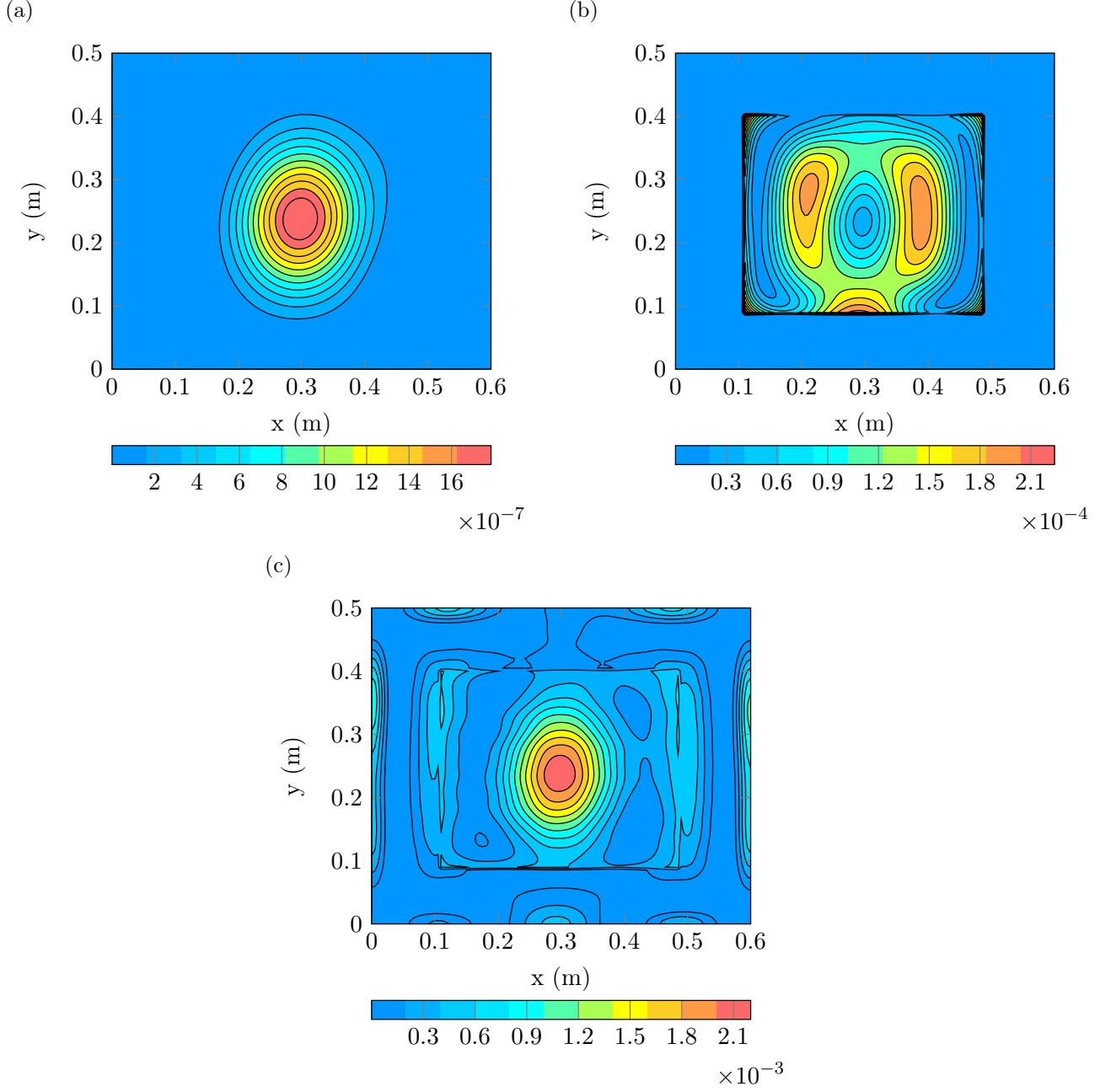
Figure 7: Maps for the designated test case at 80 Hz: (a): square velocity $\langle \dot{u}_3^2(t) \rangle$ (m^{2}s^{-2}); (b): dissipated power $\langle p_d^s(t) \rangle$ (W m^{-2}); (c): conservative strain power $2\omega \langle e_s^s(t) \rangle$ (W m^{-2}).

(a)

(b)

(c)

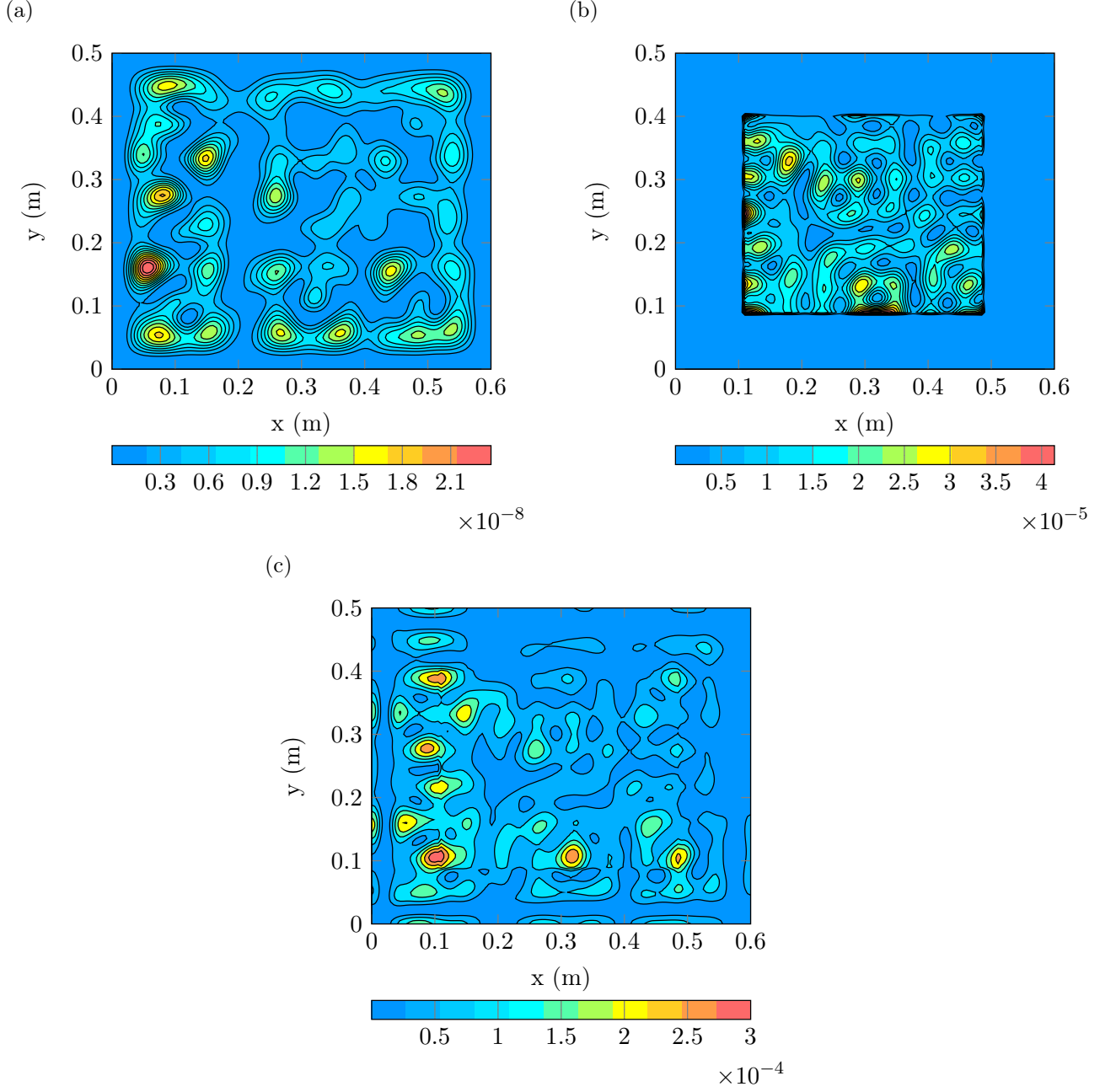Figure 8: Maps for the designated test case at 850 Hz: (a): square velocity $\langle \dot{u}_3^2(t) \rangle$ (m²s⁻²); (b): dissipated power $\langle p_d^s(t) \rangle$ (W m⁻²); (c): conservative strain power $2\omega \langle e_s^s(t) \rangle$ (W m⁻²).

13

6. Efficiency indicators

As a first introduction to the use of power and energy indicators in the damped system, this section proposes a first investigation into patch efficiency indicators from an energetic point of view. A usual indicator of sound transmission over a plate used in the literature is the transmission loss (TL), which is the ratio between the acoustic incoming power and acoustic exiting power. However, this ratio does not directly indicate the patch efficiency from a strict mechanical point of view. Indeed, the TL gives a general overview of the vibration of the plate, including the radiation efficiency of the modes and other acoustic parameters. The following proposed indicators η_1, η_2 and η_3 are only based on the damping efficiency of the patch:

$$
\begin{aligned}
\eta_1 &= \frac{\langle P_d(t) \rangle}{2\omega \langle E_k(t) \rangle} \\
\eta_2 &= \frac{\langle P_d(t) \rangle}{2\omega \langle E_s(t) \rangle} \\
\eta_3 &= \frac{\langle P_d(t) \rangle}{2\omega(\langle E_k(t) \rangle + \langle E_s(t) \rangle)}
\end{aligned}
\tag{29}
$$

Indicator η_1 is adapted to an optimization of the patch for acoustic efficiency; either the kinetic energy of the structure is considered directly related to the acoustic emission of the structure or it can be coupled with the radiation efficiency. Indicator η_2 is adapted to a mechanical optimization of the patch. Minimizing the strain energy tends to improve the mechanical behavior of the structure. Indicator η_3 is a hybrid indicator combining η_1 and η_2.

We can also notice that η_2 is similar to the indicator η as presented by Johnson and Kienholz [30]. The main difference is that η_2 takes into account the total dissipated energy while η takes only into account the energy dissipated in the viscoelastic layer.
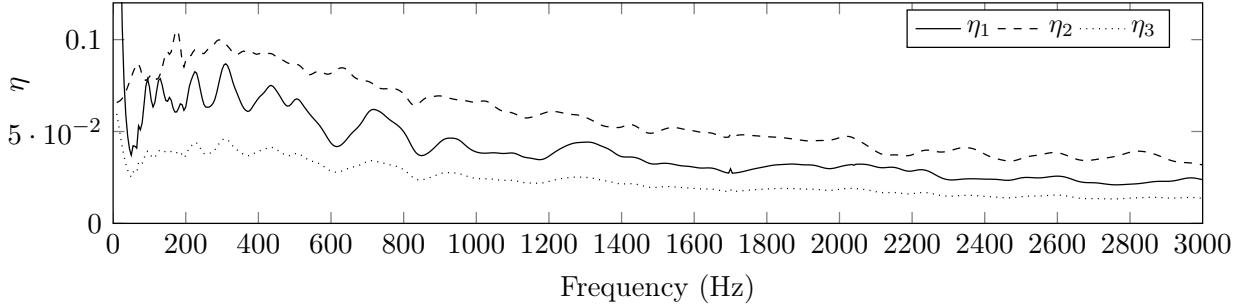

Figure 9: Ratios η_1, η_2, and η_3 over the frequency range 5Hz–3000Hz

If we analyze the general trend of the three curves in figure 9, we can see that the three indicators tend to decrease as frequency gets higher. This can be explained with the following logic:

- In a low frequency range, the deformed structure looks like the uncovered plate, and only the amplitude of the deformation is affected by the patch.

- However, in a higher frequency range, the mean square velocity over the patch surface is much lower than the mean square velocity over the rest of the plate. The patch surface almost behaves as rigid, and the rest of the plate is almost as patch free.

In conclusion, it is possible to choose one of the new optimization criteria depending on what is the primary goal of the damping patches (i.e., limiting the kinetic energy and/or the strain energy). Trying to maximize one of the proposed criteria over the frequency range with an optimization algorithm should minimize the behavior described in the previous paragraph.

7. Conclusion

Vibrations of a PCLD damped plate excited by an acoustic plane wave are studied by means of a two-dimensional, multilayer plate model. This model takes into account the kinematic and transverse shear stresses assumptions at layer interfaces. The Rayleigh-Ritz method is used to formulate the system of equations.

The present model is compared to three finite element models: a three-dimensional elasticity model (Cast3m), a three-dimensional shell model (ACTRAN), and a two-dimensional plane strain beam model (Cast3m). The present model has a significantly lower computation cost due to its two-dimensional nature. However, it is shown that it very accurately describes the behavior of the patch over the layers.

Mathematical formulas for complex mechanical power are presented, and the link with classical energies is established. Starting from the mechanical equilibrium equations, a local complex power balance is written. Its imaginary part corresponds to a conservative power balance, whereas its real part accounts for the dissipative behavior. Integration over the volume leads to a global complex power balance. Corresponding expressions involving the matrices and vectors of the discretized problem are also given.

Established formulas are used to study the conservative and dissipative energies. First, the global complex powers are computed for the three plate models over their respective valid frequency range. Second, strain energy and dissipated power are analyzed in terms of contribution of the components of the strain and stress tensors and also in terms of layers' contribution. This part of the study confirms the usual ideas concerning the behavior of PCLD patches by giving quantitative results. Finally, the in-plane distributions of powers are mapped, showing the location where dissipated phenomenon occurs and where strain energy is stored.

Three criteria based on the previous power quantities are proposed, they are plotted versus frequency for the test case. These criteria compare the dissipative power with either the kinetic energy, the strain energy, or the total energy, and can be suitable to estimate the efficiency of the damping device. Each of the criteria can be relevant depending on the type of study.

These analyses bring elements of a methodology allowing to better understand the behavior of damped structures. Such studies based on an energy approach could be useful to investigate patch design in the future.

Appendix A. Formulas for the viscoelastic material properties

Formula for Young's modulus in Pascal, f being the frequency in Hertz:

$$E(f) = 10^{(0.4884 \log(f) + 5.3848)} \tag{A.1}$$

Formula for the loss factor η , f being the frequency in Hertz:

$$\eta(f) = 10^{(0.0175 \log(f)^3 + 0.0571 \log(f)^2 + 0.0015 \log(f) - 0.0874)} \tag{A.2}$$

Acknowledgement

References

[1] Pressed Steel Company Limited and W. Swallow. An improved method of damping panel vibrations. British patent n° GB 513171 (A), 1939.

[2] M.D. Rao. Recent applications of viscoelastic damping for noise control in automobiles and commercial airplanes. *Journal of Sound and Vibration*, 262(3):457–474, 2003.

[3] H. Zheng, G.S.H. Pau, and Y.Y. Wang. A comparative study on optimization of constrained layer damping treatment for structural vibration control. *Thin-Walled Structures*, 44(8):886–896, 2006.

[4] D.H. Lee. Optimal placement of constrained-layer damping for reduction of interior noise. *American Institute of Aeronautics and Astronautics Journal*, 46(1):75–83, 2008.

[5] M. Alvelid. Optimal position and shape of applied damping material. *Journal of Sound and Vibration*, 310(4-5):947–965, 2008.

[6] C.M. Chia, J.A. Rongong, and K. Worden. Evolution of constrained layer damping using a cellular automaton algorithm. *Proceedings of the Institution of Mechanical Engineers, Part C: Journal of Mechanical Engineering Science*, 222(4):585–597, 2008.

[7] C.M. Chia, J.A. Rongong, and K. Worden. Strategies for using cellular automata to locate constrained layer damping on vibrating structures. *Journal of Sound and Vibration*, 319(1-2):119–139, 2009.

[8] R.H. Lyon. *Statistical energy analysis of dynamical systems: theory and applications*. MIT Press, 1975.

[9] D.J. Nefske and S.H. Sung. Power flow finite element analysis of dynamic systems: basic theory and applications to beams. *Journal of Vibration, Acoustics, Stress and Reliability*, 111:94–106, 1989.

[10] J.C. Wohlever and R.J. Bernhard. Mechanical energy flow models of rods and beams. *Journal of Sound and Vibration*, 153(1):1–19, 1992.

[11] Y. Lase, M.N. Ichchou, and L. Jezequel. Energy flow analysis of bars and beams: Theoretical formulations. *Journal of Sound and Vibration*, 192(1):281–305, 1996.

[12] Y.H. Park and S.Y. Hong. Vibrational power flow models for transversely vibrating finite mindlin plate. *Journal of Sound and Vibration*, 317(3-5):800–840, 2008.

[13] G. Pavic. The role of damping on energy and power in vibrating systems. *Journal of Sound and Vibration*, 281(1-2):45–71, 2005.

[14] G. Pavic. Numerical study of vibration damping, energy and energy flow in a beam-plate system. *Journal of Sound and Vibration*, 291(3-5):902–931, 2006.

[15] A. Loredo, A. Plessy, A. El Hafidi, and N. Hamzaoui. Numerical vibroacoustic analysis of plates with constrained-layer damping patches. *The Journal of the Acoustical Society of America*, 129(4):1905–1918, 2011.

[16] C.T. Sun and J.M. Whitney. Theories for the dynamic response of laminated plates. *American Institute of Aeronautics and Astronautics Journal*, 11:178–183, 1973.

[17] S.G. Lekhnitskii. Strength calculation of composite beams. *Vestnik inzhen i tekhnikov*, 9, 1935.

[18] S.A. Ambartsumyan. On a general theory of bending of anisotropic plates. *Investiia Akad. Nauk SSSR Ot Tekh. Nauk*, 4, 1958.

[19] E. Carrera. Historical review of zig-zag theories for multilayered plates and shells. *Applied Mechanics Reviews*, 56(3):287–308, 2003.

[20] H. Hu, S. Belouettar, M. Potier-Ferry, and E.M. Daya. Review and assessment of various theories for modeling sandwich composites. *Composite Structures*, 84(3):282–292, 2008.

[21] J.M. Whitney. Shear correction factors for orthotropic laminates under static load. *Journal of Applied Mechanics*, 40(1):302–304, 1973.

[22] A.K. Noor and W.S. Burton. Stress and free vibration analyses of multilayered composite plates. *Composite Structures*, 11(3):183–204, 1989.

[23] P.F. Pai. A new look at shear correction factors and warping functions of anisotropic laminates. *International Journal of Solids and Structures*, 32(16):2295–2313, 1995.

[24] N.G. Stephen. Mindlin plate theory: best shear coefficient and higher spectra validity. *Journal of Sound and Vibration*, 202(4):539–553, 1997.

[25] K.H. Lo, R.M. Christensen, and E.M. Wu. A high-order theory of plate deformation—part 1: Homogeneous plates. *Journal of Applied Mechanics*, 44(4):663–668, 1977.

[26] K.H. Lo, R.M. Christensen, and E.M. Wu. A high-order theory of plate deformation—part 2: Laminated plates. *Journal of Applied Mechanics*, 44(4):669–676, 1977.

[27] J.N. Reddy. A simple higher-order theory for laminated composite plates. *Journal of Applied Mechanics*, 51(4):745–752, 1984.

[28] E. Carrera. On the use of the Murakami's zig-zag function in the modeling of layered plates and shells. *Computers & Structures*, 82(7-8):541–554, 2004.

[29] J.L. Guyader and C. Lesueur. Acoustic transmission through orthotropic multilayered plates, part i :plate vibration modes. *Journal of Sound and Vibration*, 97:51–68, 1978.

[30] C.D. Johnson and D.A. Kienholz. Finite element prediction of damping in structures with constrained viscoelastic layers. *American Institute of Aeronautics and Astronautics Journal*, 20:1284–1290, 1982.